Distinguishing Propagating Waves and Standing Modes: An Internal Wave Model*

M. BENNO BLUMENTHAL

Lamont-Doherty Earth Observatory of Columbia University, Palisades, New York

MELBOURNE G. BRISCOE

NOAA, National Ocean Service, Silver Spring, Maryland

(Manuscript received 1 February 1993, in final form 12 August 1994)

ABSTRACT

This paper examines high-frequency (0.1–0.5 cph) internal waves, waves previously characterized by the Garrett and Munk spectral fits (GM72, GM75, GM79) as being vertically symmetric propagating waves (or equivalently "smeared" standing modes—GM72). Coherences at large vertical separations measured with deep sea moorings show significant differences from the GM79 predictions. The differences can be explained by modifying the purely propagating model to one that includes the spectral truncation and phase locking associated with a spectrum of standing modes. A model consisting of only standing modes, however, is also inadequate, whereas a more general spectral model, which effectively allows both propagating waves and standing modes, is not. These results show that much of the simplicity of the GM79 spectral fit can be attributed to lack of spectral resolution in the set of measurements to which the GM models were fit. The GM79 simplicity is not an intrinsic property of the internal wave field.

1. Introduction

It has been primarily a matter of taste as to whether vertically standing modes or vertically propagating waves are used to describe the vertical structure of oceanic motions, since both the set of all vertically propagating waves and the set of all standing modes are by themselves complete; that is, arbitrary linear motions can be described by a sum of one set or the other. In interpreting spectra, however, there is a useful distinction between the waves and modes: statistically independent standing modes cannot carry energy vertically, and statistically independent propagating waves cannot show any phase locking to particular depths (e.g., they cannot satisfy top and bottom boundary conditions). We present evidence here that a simple propagating wave model is inadequate for high-frequency internal waves. The inadequacies of such a model can be remedied by considering standing modes. It is better, however, to describe the field as a *mixture* of propagating waves and standing modes, better because it more closely fits the observations and because it is more self-consistent theoretically. While this discussion deals with high-frequency (0.1–0.5 cph) internal waves, the general distinctions between vertically propagating waves and standing modes apply to other scales and wave systems as well.

The structure of this paper is as follows. Section 2 reviews internal waves as they are summarized by the Garrett and Munk (GM) internal wave papers (Garrett and Munk 1972, henceforth GM72; Garrett and Munk 1975, henceforth GM75; Munk 1981 henceforth GM79). The GM models were empirical fits that embodied much of what was known about internal waves. Section 3 describes the subset of the Pacific Equatorial Dynamics (PEQUOD) Experiment current meter array used to analyze the internal wave field and presents a brief description of the background state for these waves. Section 4 compares the vertical coherence observed in PEQUOD with that expected from GM79, showing that there are distinct differences at separations not available during the formulation of the GM models. Section 5 derives a modified version of the GM79 vertical coherence prediction that better explains the features seen in the PEQUOD and LOTUS coherences. The modifications consist of changing the essentially purely propagating model of GM to a model that includes both the spectral truncation and the phase locking associated with a spectrum of standing modes.

Section 6 presents coherence and phase from the LOTUS experiment (Briscoe and Weller 1984) measurements, which show similar features to those seen in the PEQUOD data. Section 7 briefly summarizes the coherence measurements and the modifications to

* Lamont-Doherty Earth Observatory Contribution Number 5242.

Corresponding author address: Dr. M. Benno Blumenthal, Lamont-Doherty Earth Observatory, Columbia University, Palisades, NY 10964.

the GM coherence model, showing that while the modified model explains features the original model could not, the model is still inadequate in some respects.

The point here is not whether the GM models are exactly right or quite wrong but rather that they are commonly used as a first-order description of the internal wave field, so it is best to understand the models and their limitations.

2. Internal waves

Two decades ago, Garrett and Munk published a paper (GM72) that used linear dynamics to synthesize a frequency–wavenumber energy spectrum for internal waves, a spectrum that fits all the available internal wave measurements reasonably well. A key result of GM72 is that the spectral level and scales of the internal wave field are essentially the same throughout much of the world's pelagic oceans. This apparent universality of the internal wave spectrum has meant that the data from many different places have been compared to the GM72 spectrum and have led to only small changes in the GM model (Garrett and Munk 1975; Cairns and Williams 1976; Munk 1981). But a strictly universal model is overly simple: such a model, for example, does not allow localized sources and sinks of energy, a spatial diversity which would be expected given the diversity of processes occurring in the ocean (Wunsch 1976). Later observations have, in fact, demonstrated that there are significant variations in the internal wave field (Wijesekera and Dillon 1991; Eriksen 1988; Briscoe 1984; Levine 1984; Pinkel 1984; Roth et al. 1981; among others). In spite of these results, the GM models have survived in large part intact.

The current form of the Garrett and Munk spectrum (GM79) describes the internal wave energy E_{IW} as a function of frequency ω and mode number j:

$$E_{IW}(\omega, j) = N(z)E(\omega, j) = N(z)\tilde{E}B(\omega)H(j); \quad (1)$$

that is, the internal wave energy at any particular depth is factored such that it is proportional to the local buoyancy frequency $N(z)$, a function of frequency $B(\omega)$, and a function of vertical mode number $H(j)$. The factoring into separate functions of mode number and frequency has no theoretical basis; much of the data considered in the GM papers was in frequency space and is thus consistent with such a factoring.

In particular,

$$N\tilde{E} = 30(N/N_0)\ \text{cm}^2\ \text{s}^{-2} \quad (2a)$$

$$B(\omega) = \frac{2f}{\pi\omega\sqrt{\omega^2 - f^2}}, \quad \int_f^N B(\omega)d\omega = 1 \quad (2b)$$

$$H(j) = \frac{(j^2 + j_*^2)^{-1}}{\sum_1^\infty (j^2 + j_*^2)^{-1}}, \quad \sum_1^\infty H(j) = 1, \quad (2c)$$

where $j_* = 3$ and $N_0 = 3$ cph.

Desaubies objects to this sum of modes formulation (2c) on the grounds that wave–wave interactions prevent discrete normal modes from forming (Desaubies 1976; McComas and Bretherton 1977). He then suggests a continuous form of the GM79 wavenumber spectrum with $H(K)$ given by

$$H(K) = \frac{(2/\pi)K_*}{K_*^2 + K^2}, \quad (3)$$

where

$$K_* = \pi \frac{\sqrt{w^2 - f^2}}{D\bar{N}} j_* \quad (4)$$

(D is the depth of the ocean).

Several nonlinear mechanisms prevent mode formation at high wavenumber. *Parametric subharmonic instability* prevents modes for $j > 25$ (Garrett 1991). *Elastic scattering* prevents modes by mixing upward and downward propagating waves (McComas and Bretherton 1977). But in interpreting data this is misleading because the internal wave spectrum has most (50% as approximated by the Desaubies spectral form, for example) of the energy in modes 0–3. Mode 3 has 1½ wavelengths between the top and bottom; thus there is little potential for scattering. Furthermore, low wavenumbers have higher group velocities, so they are more efficient carriers of energy. While rapid interactions strongly affect high wavenumbers and thus can determine the overall shape of the wavenumber spectrum, high wavenumbers contain and carry relatively little energy. Thus, an analysis that focuses on low wavenumbers, wavenumbers relatively unaffected by rapid interactions, will explain most of the energy density and fluxes.

Finally, as the PEQUOD data will demonstrate, (3) is now measurably different from (2c) and is not consistent with the data. Also, not consistent are some of the simplifying assumptions used in GM79 to convert $E(\omega, j)$ to a measurable quantity, the moored sensor vertical coherence (MVC). In this paper, we find significant deviations between data and the GM79 MVC prediction. Those differences are at the large separations for which GM had no measurements; that is, these are not differences with the data upon which GM79 is based, but rather with the forms chosen in GM79, forms that predict values extrapolated beyond the original data.

3. Data description

a. PEQUOD current meter array

The primary objective of PEQUOD was to understand the dynamics of the equatorial ocean, deep equatorial dynamics in particular (Eriksen 1985). Portions of the PEQUOD current meter array are used in this paper to study high-frequency internal waves. A com-

TABLE 1. PEQUOD time series table: ocean depth at Q is 4250 m; ocean depth at U is 4400 m.

Label	Latitude	Longitude	Start date	Length (h)	Depth (m)
Q101	0°00.3'S	144°40.9'W	24 Jan 1981	9251	514.7
Q102 (TP)				9241	589.7
Q103				9100	614.7
Q104 (TP)				9100	664.6
Q106 (TP)				9100	1590.0
Q107				8834	1615.0
Q108 (TP)				9100	1664.9
Q109				8802	3015.0
Q110 (TP)				9100	3090.0
Q111				9248	3114.9
U201	0°20.7'N	144°32.6'W	18 Feb 1982	8978	495.3
U202 (TP)				8979	570.4
U203				8978	595.4
U204 (TP)				6383	645.4
U205				8979	1495.7
U206 (TP)				8979	1570.8
U207				8979	1595.8
U208				8979	1645.8
U209				8979	2996.3
U210 (TP)				8979	3071.4
U211				8979	3096.4
U212 (TP)				8979	3146.4

plete description of the array, its design, and data return are given in Eriksen (1985). (The instrumental depths and data return are given here in Table 1; horizontal placements in Fig. 1.) This paper uses data from the two central moorings (lettered Q–U). The central moorings were set in relatively flat areas and have 12 instruments each (Aanderaa current meters alternating with temperature–pressure recorders) clustered at three depths; thus there is resolution of both fairly short [O (50 m)] and long [O (1000 m)] vertical scales.

Aanderaa current meters are rotor–vane instruments that record temperature, rotor count, and direction once per sampling interval. (In PEQUOD, this was once per hour.) Differenced rotor counts divided by the sampling interval provide an average speed; which is combined with the instantaneous direction measurement to get velocity components. This scheme results in aliasing of direction, which restricts the extent to which internal wave information can be extracted from the data. The aliasing enhances autospectra near the sampling frequency: this tends to lower coherence at high frequencies. Since our results consist of high coherence and do not show a strong high-frequency dependence, the effect is not important. Furthermore, the LOTUS data are based on vector-averaging instruments and are not subject to such aliasing.

The temperature–pressure recorders are discussed by Wunsch and Dahlen (1974). The major instrumental distortion is a delayed response of the thermistors relative to the pressure sensor (due to the thermal

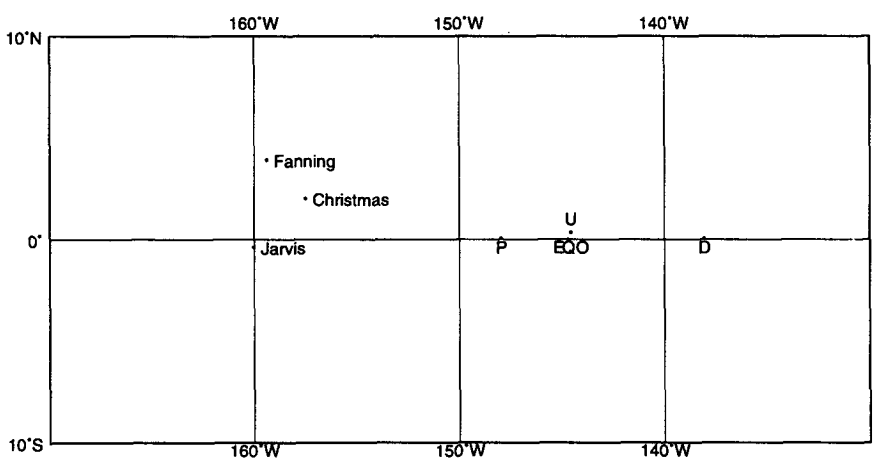

FIG. 1. PEQUOD mooring summary.

mass of the sensor). For the instruments used in PEQUOD the delay (*e*-folding time) is either 3 minutes or 23 minutes (depending on the instrument), much greater than the delay of the Aanderaa temperature sensors (which is on the order of seconds). Because an *e*-folding time of 23 minutes corresponds to a phase lag as large as 50° at a period of 2 hours, the temperature records were processed to remove the effects of thermal lag with the transfer function

$$T_c(\omega) = (1 + i\omega\tau)T_m(\omega), \qquad (5)$$

where $T_m(\omega)$ are the Fourier coefficients as calculated from the data, $T_c(\omega)$ are the corrected Fourier coefficients that are subsequently averaged to calculate spectra, ω is the frequency, and τ is the *e*-folding time for the thermistor.

b. Background state for the internal wave field

In addition to the moored array data, there are Whitehorse Velocity Dropsonde profiles taken in January 1981, February 1982, and April 1982 (Voorhis et al. 1984). The 28 profiles taken near the sites of the moorings were used to calculate an average buoyancy frequency profile $N(z)$ (Fig. 2) and average velocity profiles $U(z)$ (Fig. 3). The velocity profiles give a detailed vertical structure that helps us estimate the effect of the mean velocity shear on the internal wave field.

Figure 4 shows the Doppler shift for three modes. The first ten modes are unaffected by Doppler shifts within the depth range of the current meters (500–3200 m). All modes except the first have critical layers in the undercurrent; hence only the first mode will be influenced directly by the surface boundary condition.

The inverse root Richardson number measures a purely local distortion in the polarization relations (Blumenthal 1987). Figure 4 shows that the ratio reaches 0.5 at several depths that are near the depths of PEQUOD current meters, suggesting that the mean shear can affect some of the measurements at those locations. These particular changes in polarization, however, have no effect on vertical coherences like those discussed in this paper (Blumenthal 1987).

4. Vertical coherence comparison of PEQUOD data with GM79

The moored vertical coherences provide a check of the GM choice of wavenumber dependence $H(j)$. Comparison of the PEQUOD data with the GM79 model shows two quite distinct results. For short separations the coherences observed with the PEQUOD array are essentially the same as those predicted by GM79, suggesting that the short-separation temperature coherence can be modeled as being due to a field of internal waves plus some finestructure that is advected vertically past the mooring. But for longer separations the results from PEQUOD are distinctly different from the GM79 prediction. This latter result is not particularly surprising, since the GM79 model is based on coherences over relatively short separations. The PEQUOD–GM79 differences show that there are aspects of the internal wave field that are measurable but are not included in the GM models.

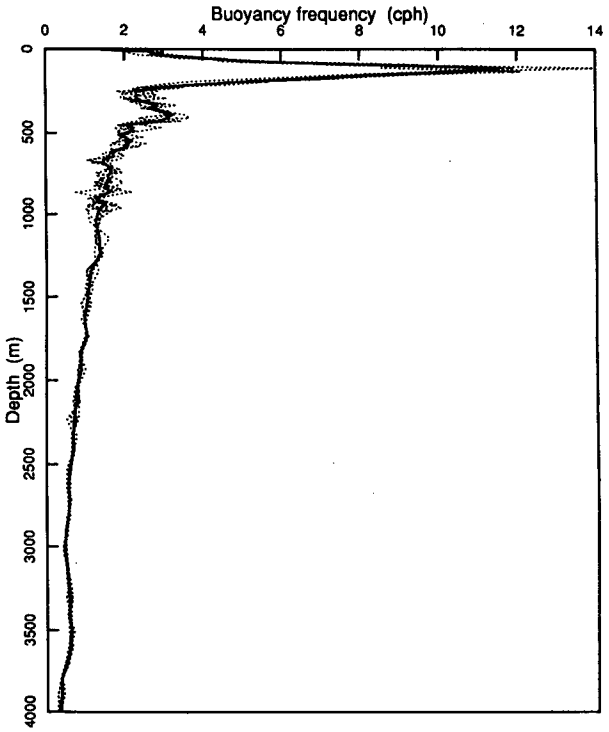

FIG. 2. Buoyancy frequency profiles from Whitehorse data. Solid: averaged over all 28 profiles, dotted: averaged over each location separately.

Here the WKBJ scaled separation ζ is defined as

$$\zeta(z_1, z_2) = \frac{1}{1 \text{ cph}} \int_{z_1}^{z_2} N(z')dz', \qquad (6)$$

where z_1 is the depth of the first instrument, z_2 is the depth of the second, and $N(z)$ is in cycles per hour (Desaubies 1975).

The WKBJ separations available from the Q and U moorings fall into three distinct ranges: short (10–300 m), medium (1000–1600 m), and long (2250–2600 m). The medium range measurements can be further split into two subgroups: the 900–1100-m spacings between the center and bottom group of instruments and the 1200–1600-m spacings between the center and top groups of instruments. Thus, although the center group of instruments is actually closer to the top group, it is closer to the bottom group in a WKBJ-scaled sense.

The PEQUOD short-separation coherences are indistinguishable from Webster's rule (cf. GM72), so they are consistent with midlatitude observations (Blumenthal 1987). This suggests that the short-sep-

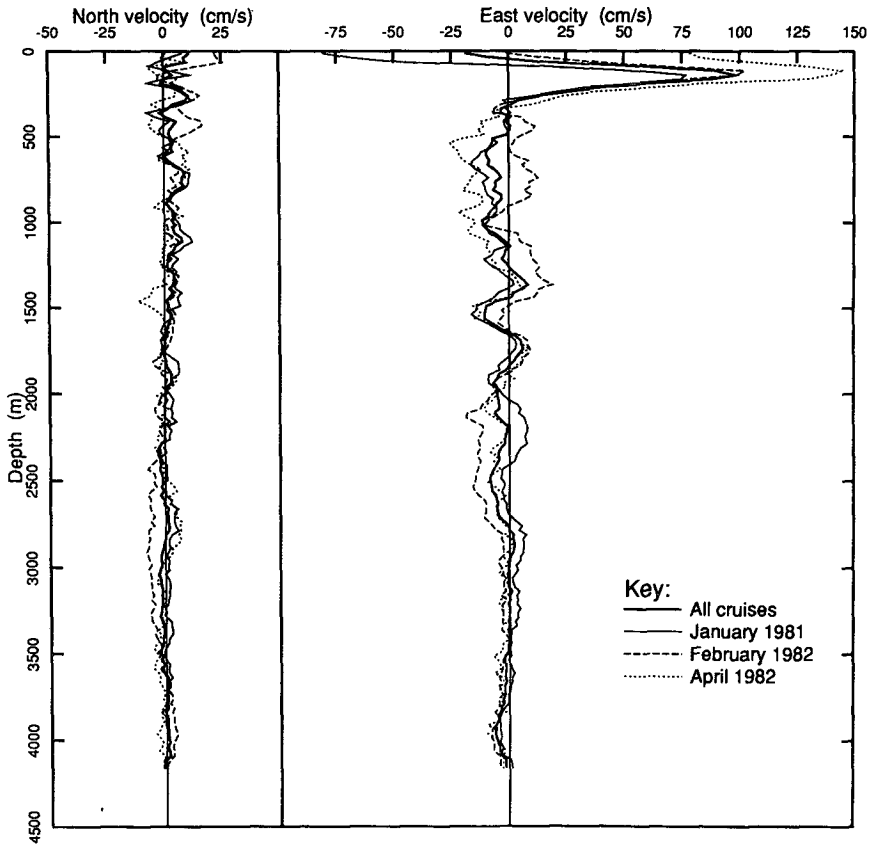

FIG. 3. Whitehorse velocity profiles at 0°, 145°W. Solid: averaged over all nine profiles, other: profiles averaged over single cruises. Comparison of the mean curves with the subset curves shows that there is quite a bit of time variability.

aration temperature coherence can be modeled as being due to a field of internal waves plus some finestructure that is advected vertically past the mooring (GM72). In contrast, while examining equatorial Indian Ocean data (from INDEX), Wunsch and Webb (1979) saw almost no vertical coherence above 0.5 between velocity sensors that had as little as 100-m separations. Even at midlatitudes, Briscoe (1977) finds relatively low velocity coherence, though he is considering much shorter separations (2–6 m). Presuming that these drops in short-range coherence are in fact due to finestructure, these results imply that there is some variability in the finestructure found at various sites. Velocity profiles in the PEQUOD area (Fig. 3) show considerable velocity structure at larger than finescales (Voorhis et al. 1984; Luyten and Swallow 1976), but are not finestructure measurements. In this paper we will focus on the large separation coherences.

Coherences calculated from the PEQUOD measurements at 1000-m vertical separations are distinctly different from GM predictions, which were based on separations no larger than 140 m. Figure 5a shows temperature coherences calculated from the first-year Q mooring data plotted against linear axes (frequency symbols are given in Table 2). Figure 5a shows that the measured temperature coherences at mooring Q are 0.2 ± 0.08 at 1000 m; all these measurements are significantly higher than the 0.1 predicted by GM. Similar results are obtained from the second-year U mooring data. Unlike smaller separations, the frequency dependence is weak and not particularly systematic. At slightly longer separations (1200–1600 m), many measured coherences exceed the GM prediction; in particular most of the estimates in the bin centered at 0.158 cph are significant, but there are also many estimates indistinguishable from zero. There are a few significantly nonzero coherences at 2500-m separations as well; none of them correspond to 0.158 cph, the frequency least susceptible to aliasing.

In the absence of finestructure, the GM model predicts that the coherence calculated between vertically separated velocity sensors will be identical to the coherence calculated between vertically separated temperature sensors. While differences in velocity and temperature finestructure can degrade coherence differently in the two fields (Briscoe 1975, 1977), finestructure does not lead to enhanced coherence at long (or short) separations.

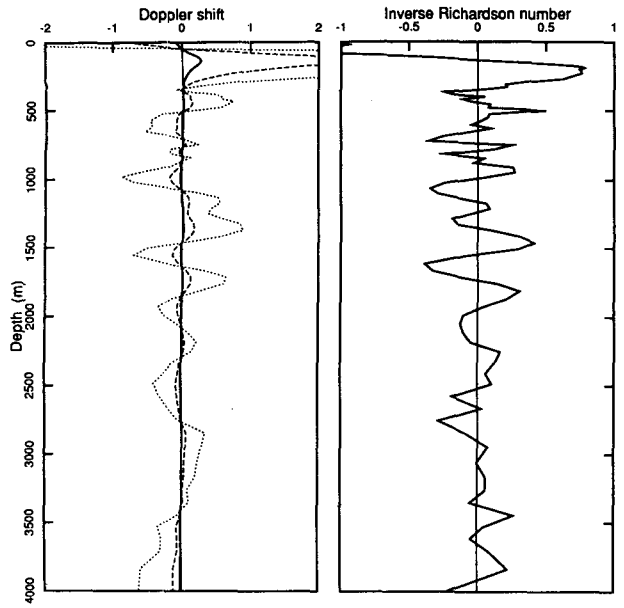

FIG. 4. Doppler shifts and inverse root Richardson number: The left plot gives the normalized maximum Doppler shift $d = u/c_i$ as a function of depth for modes 1 (solid), 10 (dashed), and 50 (dotted). $d = \pm 1$ corresponds to a *critical* layer. The right plot gives the signed inverse root Richardson number $\lambda = u_z/N$ as a function of depth (the strength of the effect on internal waves does not depend on wavenumber). Both plots are computed from a spline fit to the average of the zonal (east) velocity profiles listed in Fig. 3: the root Richardson number plot also uses a spline fit to the buoyancy frequency plotted in Fig. 2. The plots show that for depths below 500 m, Doppler shifts are only important for high modes, while the shear (root Richardson number) effects are important at certain depths for all wavenumbers.

The PEQUOD velocity coherences at long separations are distinctly different from both the GM predictions and the temperature coherences. Figure 5c gives the moored vertical coherence as calculated from the first-year Q mooring zonal velocity data, and figure 5d gives the same as calculated from the second-year U mooring data. Figures 5e and 5f give the corresponding plots for the meridional velocity. The estimates at 1000-m separation are centered about or below the GM prediction, quite unlike the temperature coherence. But even more striking is the fact that the coherence increases as separations increase above 1000 m. In fact, the velocity coherences at 2500-m separation are as strong as the temperature coherences at 1000-m separation. The implied middepth minimum in the coherence (since 1000-m separations all include middepth instruments) suggests that the energy that is responsible for the coherence has some modal structure that includes a node at middepths. This hypothesis is supported by the phase plots for velocity and temperature.

As might be expected from the coherence magnitudes, the velocity phase differences are distinctly different from the temperature phase differences. Figures 6a,b give the phase differences calculated from the Q1 temperature data and the U2 temperature data, respectively. The plots show that while all of the temperatures have phase differences indistinguishable from zero at 1000-m separation, the significant coherences at 2500 m have phase differences close to 180°. The two frequency bins that have significant phases at 2500-m separation are not contiguous: one is centered at 0.225 cph and the other is centered at 0.358 cph, and the intervening bin does not show any significant phase differences above 1200-m separation. The temperature phase differences at 1500-m separations are harder to characterize. The temperature phase difference for 0.158 cph is zero for both the Q1 and U2 data. The phase difference for 0.225 cph is slightly less than −45°, which is statistically indistinguishable from zero. Finally, one of the two frequency bins that have significant phase differences at 2500-m separation has the same phase difference (180°) at approximately 1500-m separations, and the highest frequency bin has 180° phase differences at 1500 m and no significant coherence at 2500-m separation. While there are some differences in the temperature phase structure as a function of frequency, there is no systematic trend with increasing frequency. Note that all of the complicated phase structure is at separations where the coherence is relatively small. At a particular frequency, small coherence means that only a small fraction of the energy is involved in causing such motions, and that not modeling such a feature will only make a small contribution to the model–data misfit. Thus, a simple characterization of the temperature data could ignore those complications and simply say that the coherence falls off from 0.2 to 0.1 between a separation of 1000 m and a separation of 1500 m, and the phase differences for all separations are indistinguishable from zero.

Like the velocity coherence plots, the velocity phase plots differ from their temperature counterparts. Figures 6c–f show the phase as a function of separation calculated from zonal and meridional velocity data from both years. The meridional velocity phases are quite simple to characterize: all separations greater than 1000 m have 180° phase differences. The phase differences calculated from zonal velocities are somewhat different in that, while the significant phases corresponding to separations greater than 1200 m are all 180° ± 45°, the phase difference at 1000-m separation is close to zero. Note that the U2 zonal velocity data have very few significant phases, none of which are at 1000 m, so the phase difference at 1000 m is not a very robust result. Thus, a simple characterization of the velocity data is that the coherence rises from approximately zero at 1000-m separation to 0.2 at 2500-m separation, with a phase difference of 180° for all separations greater than 1000 m. This is exactly opposite to the simple characterization of the temperature coherence and phase where the coherence for long separations decreases from 0.2 at 1000-m separation to

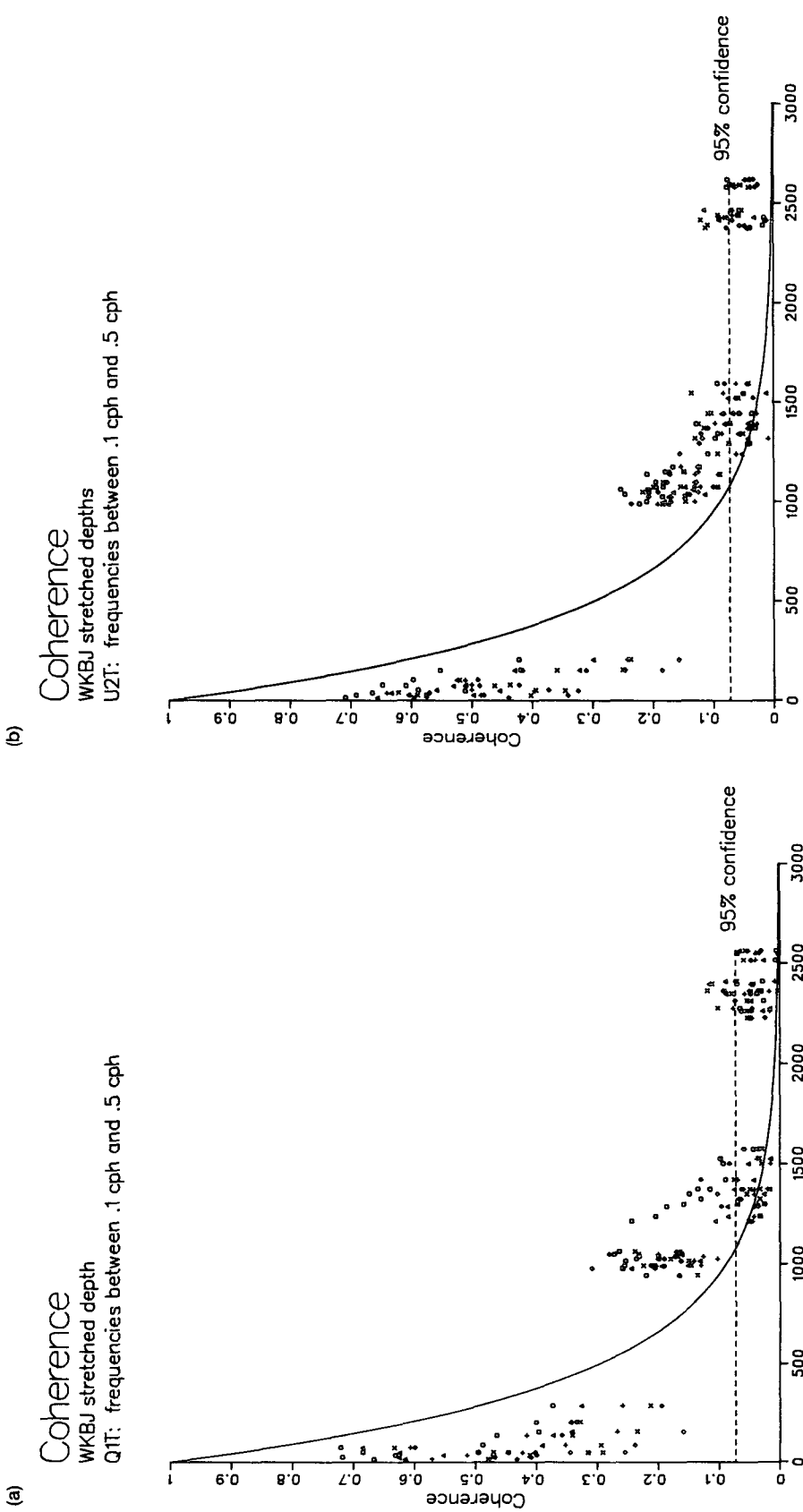

FIG. 5. Vertical coherence of temperature and velocity calculated from PEQUOD data. Each symbol corresponds to a different frequency bin (see Table 2). The lowest frequency bin is centered at 0.158 cph. The frequency bin width is 1/15 cph. The degree of averaging N_r is 576 for each estimate, and the corresponding 95% zero significance level is given by the dashed line. The solid curve is the GM prediction. The plots are (a) temperature coherence Q1 and (b) U2, (c) zonal-velocity coherence Q1, (d) and U2, and (e) meridonal-velocity coherence Q1 and (f) U2.

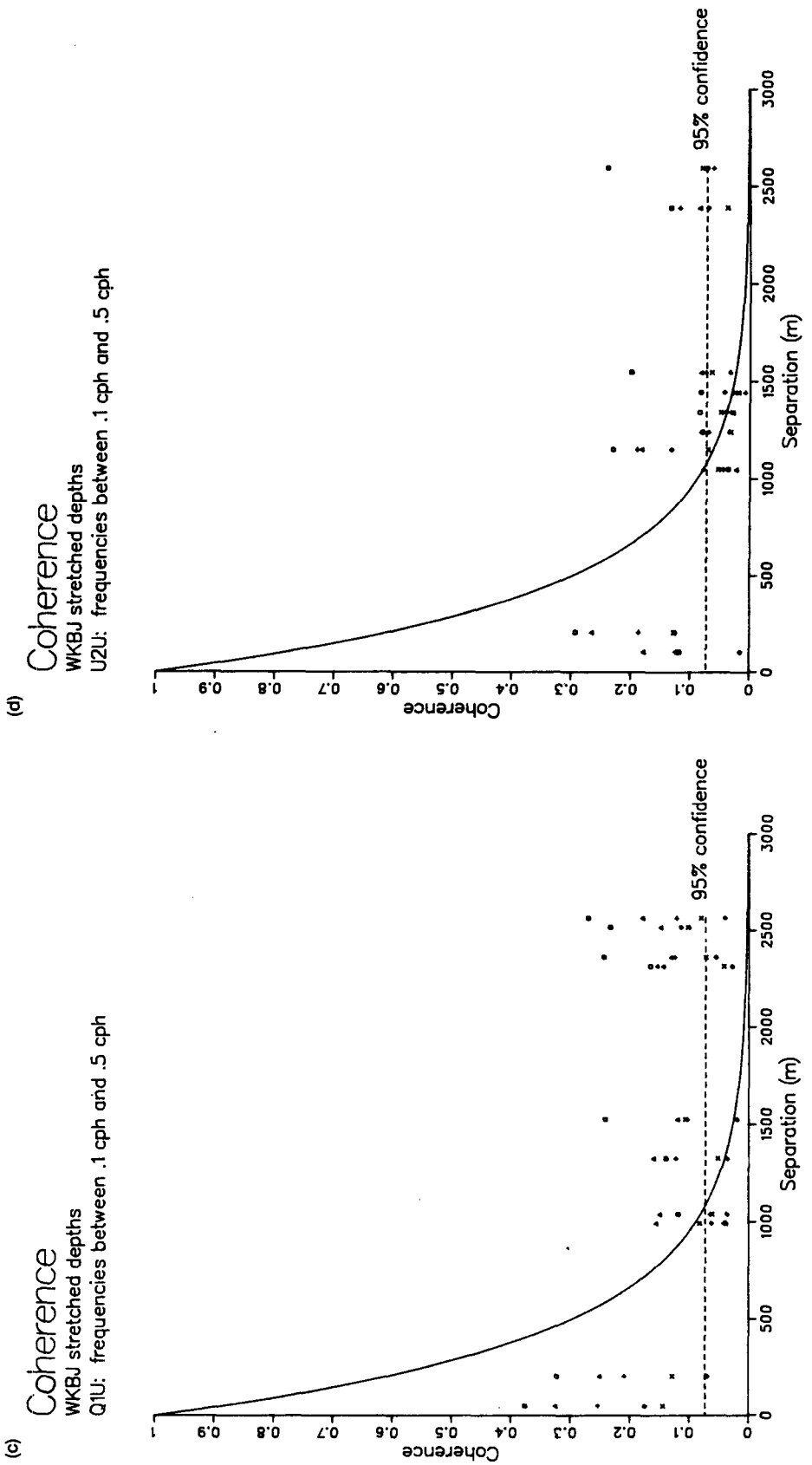

FIG. 5. (*Continued*)

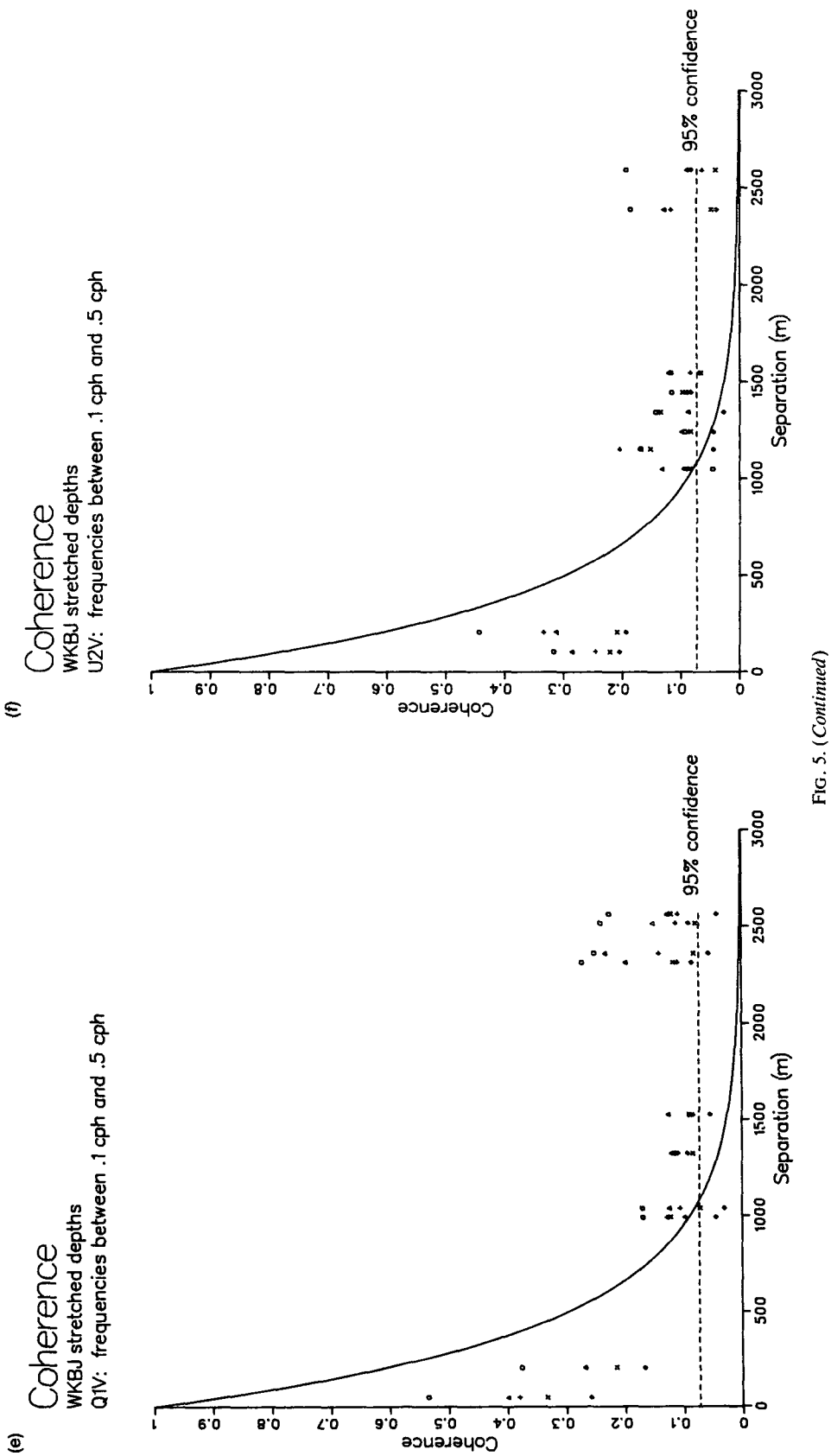

FIG. 5. (*Continued*)

TABLE 2. Frequency symbols for the PEQUOD coherences and phases.

Symbol	Frequency
□	.1583 cph
△	.2250 cph
+	.2916 cph
×	.3583 cph
◇	.4250 cph

0.1 at 1500-m separation, and there is zero phase lag for all separations.

These coherence structures represent significant deviations from GM. The GM79 wavenumber parameterization is based on measurements with separations 140 m and less (Cairns and Williams 1976; Briscoe 1975). Thus, the predictions implicit in GM79 for 1000 m and greater separations are extrapolations well beyond the GM79 observational basis. It would be quite surprising if the GM model could predict accurately at large separations.

5. An extended spectral model

This section develops the linear internal wave theory with a precise treatment of top and bottom boundary conditions, showing that unlike purely propagating waves, vertical modes lead to nonzero coherence at large separation with velocity–temperature differences of the same character as the PEQUOD observations.

GM72 uses linear internal wave dynamics to devise a unified model for spectral measurements of internal waves where the data is gathered by a variety of sensors: moored, towed, dropped, etc. This synthesis is done by using the dispersion relation to relate frequency, horizontal wavenumber, and vertical structure, and using polarization relations to relate measurements of displacement and horizontal velocity. Both the dispersion relation and the polarization relations are results of seeking wavelike solutions to the equations of motion.

a. Polarization relations and vertical structure

The linearized f-plane Boussinesq perturbation equations are

$$u_t - fv + p_x = 0 \tag{7a}$$

$$v_t + fu + p_y = 0 \tag{7b}$$

$$w_t - b + p_z = 0 \tag{7c}$$

$$b_t + N^2(z)w = 0 \tag{7d}$$

$$u_x + v_y + w_z = 0, \tag{7e}$$

where b is the buoyancy perturbation and p is the pressure perturbation divided by the mean density.

Table 3 translates the notation of GM72 to that used here—a notation more common at present.

Since the coefficients of the equations are independent of time t and horizontal position x, y, there are solutions wavelike in x, y, t with each also a function of vertical position z. It is easy to verify that those solutions are given by these *polarization relations:*

$$\begin{bmatrix} u \\ v \\ w \\ p \\ b \end{bmatrix} (x, y, z, t) \equiv \mathbf{u}(x, y, z, t) = \mathbf{p}(z, \omega, k, l) \times \alpha(z)\hat{A}(\omega, k, l)e^{i(kx+ly-\omega t)}, \tag{8a}$$

where $(k, l) = K(\cos\theta, \sin\theta)$,

$$\mathbf{p}(z, \omega, k, l) = \begin{bmatrix} \left(i\cos\theta - \dfrac{f}{\omega}\sin\theta\right)\dfrac{1}{K}\partial_z \\ \left(i\sin\theta + \dfrac{f}{\omega}\cos\theta\right)\dfrac{1}{K}\partial_z \\ 1 \\ i\dfrac{(\omega^2 - f^2)}{\omega K^2}\partial_z \\ -\dfrac{i}{\omega}N^2(z) \end{bmatrix}, \tag{8b}$$

and $\alpha(z)$ is a solution to the *vertical structure equation*

$$\alpha_{zz} + m^2(z)\alpha = 0, \tag{9a}$$

where

$$m^2(z) = \frac{N^2(z) - \omega^2}{\omega^2 - f^2}K^2. \tag{9b}$$

The vertical structure equation has two solutions for each ω and total wavenumber K. Normally at this point one makes one of two choices: modes or propagating waves. Instead, we postpone this decision by imposing the single condition that $\alpha(z)$ be upward propagating at the bottom z_D; namely,

$$\alpha_z(z_D) = im(z_D)\alpha(z_D) \tag{10}$$

[$\alpha(z_D)$ is a real constant] and writing any particular solution as

$$G(z) = A\alpha(z) + B\alpha^*(z). \tag{11}$$

This allows us to talk about an upward propagating wave ($B = 0$), and downward propagating wave ($A = 0$), or a modal solution ($B = -A$). [See Philander (1978), Gent and Luyten (1985), or Blumenthal (1987) for a more complete development of non-WKBJ propagating waves.]

b. Spectra

The phase plots (Fig. 6) show phases that differ significantly from both 0 and 180; such phases cannot be

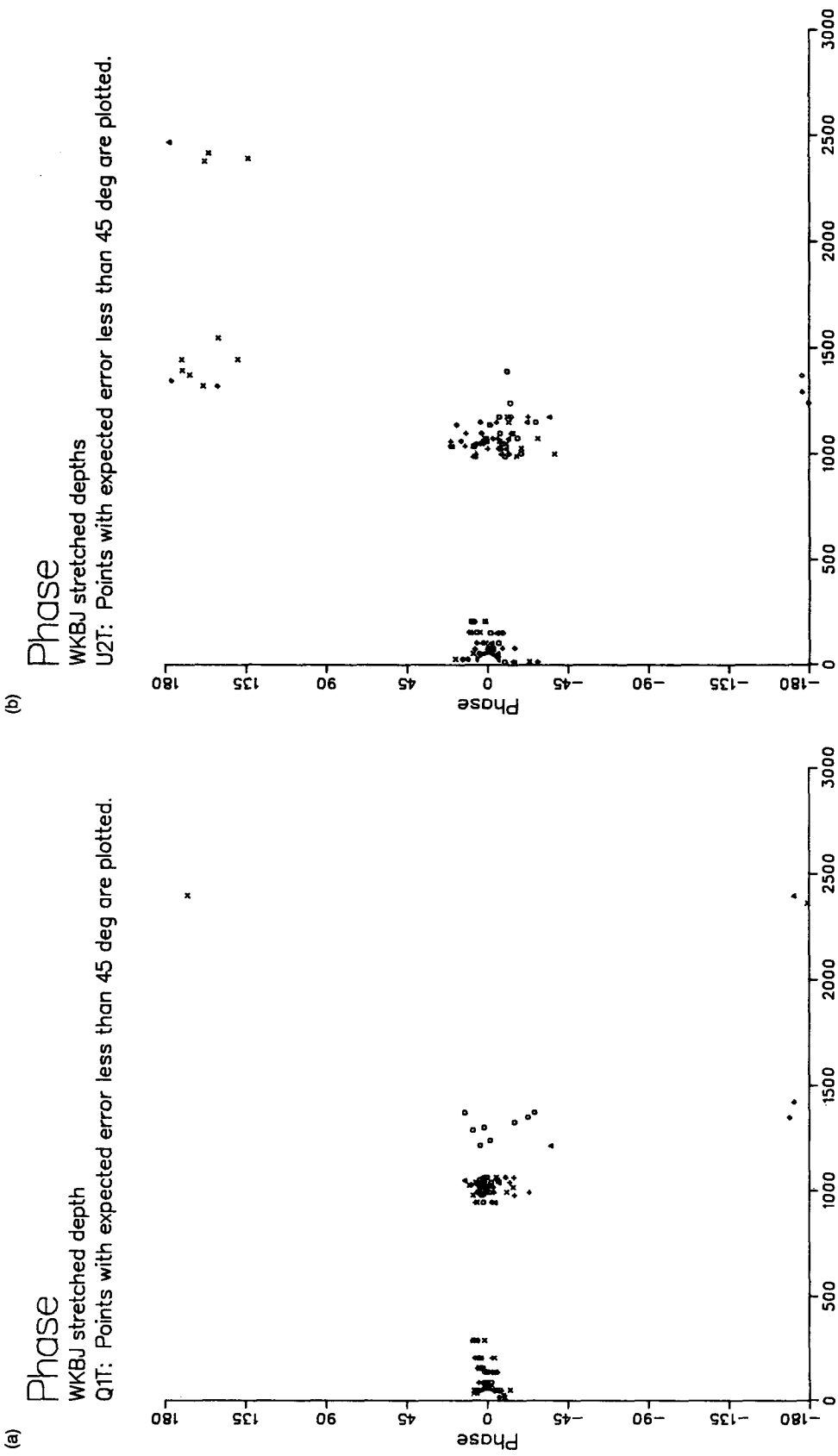

FIG. 6. Vertical phase difference calculated from PEQUOD data as a function of WKBJ-stretched separation for frequencies between 0.1 cph and 0.5 cph. Each symbol corresponds to a different frequency bin. The lowest frequency bin is centered at 0.158 cph. The frequency bin width is $1/15$ cph. The degree of averaging N_r is 576 for each estimate; error bars are not shown, but rather only points with uncertainties less than 45° are plotted. The plots are (a) temperature phase Q1 and (b) U2, (c) zonal-velocity phase Q1 and (d) U2, and (e) meridonal-velocity phase Q1 and (f) U2.

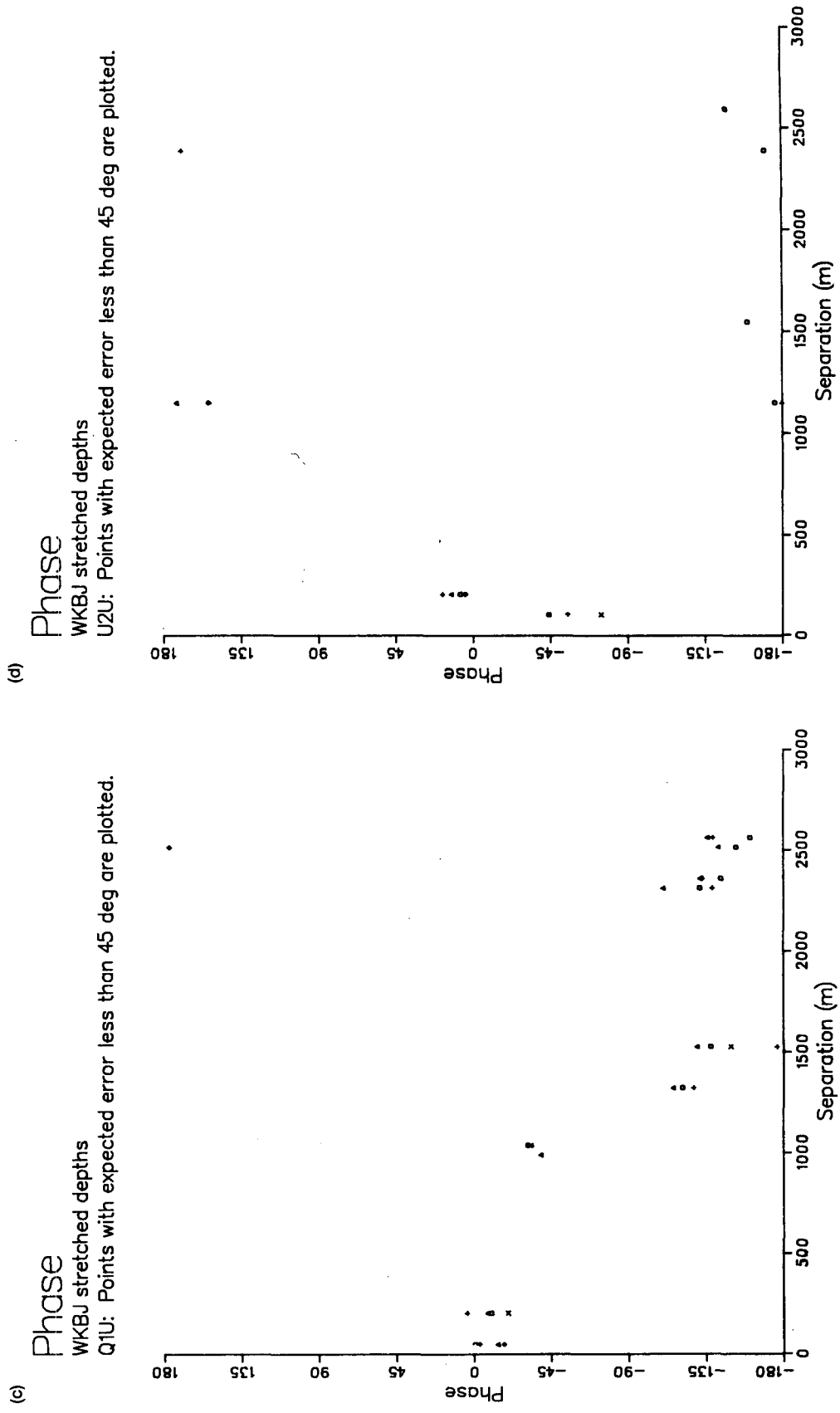

FIG. 6. (*Continued*)

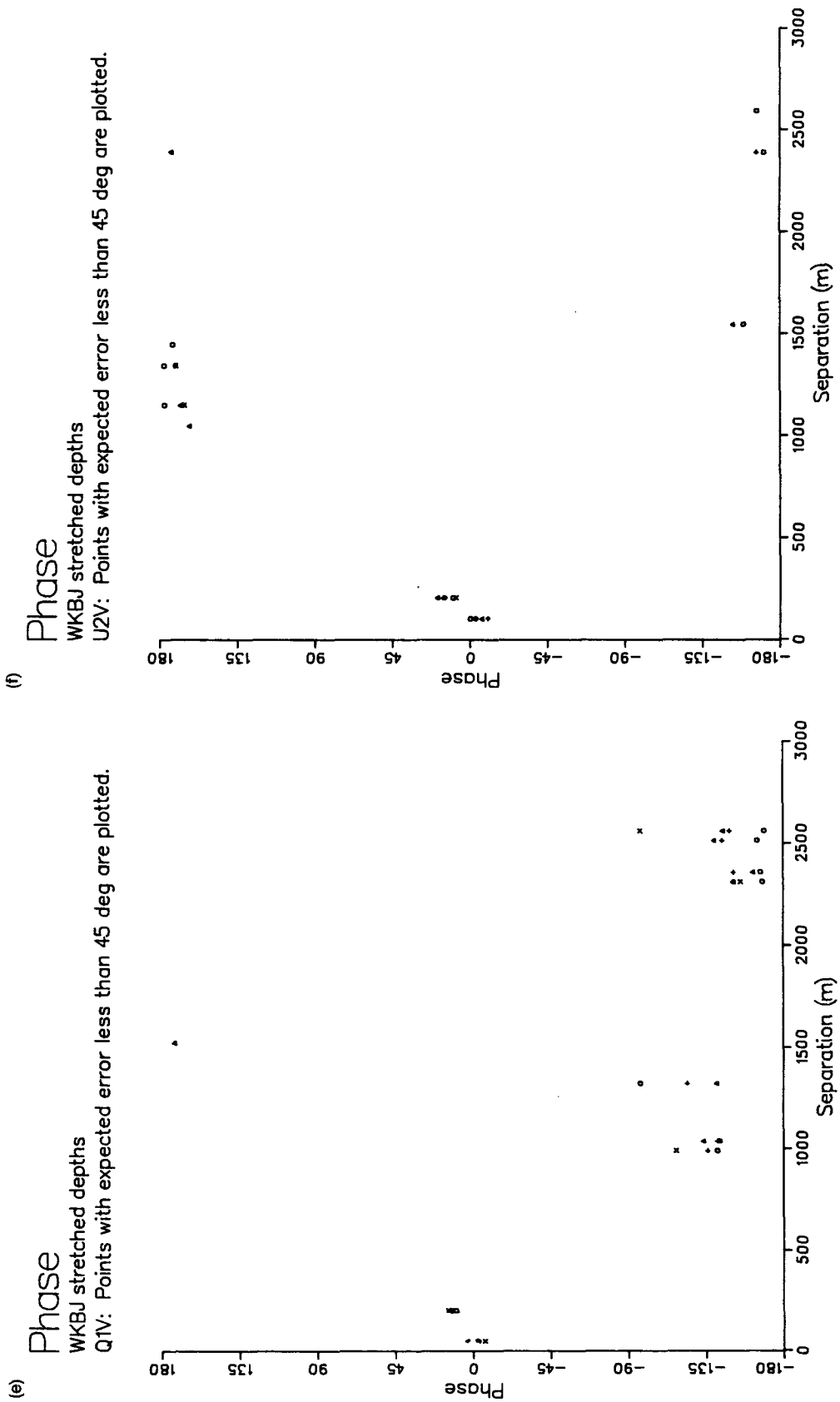

FIG. 6. (*Continued*)

TABLE 3. Notation and GM72 equivalents.

Variable	GM72	Description
$N(z)$	$\hat{n}$	Buoyancy frequency
u	u_1	Zonal velocity
v	u_2	Meridional velocity
w	v	Vertical velocity
z	$-y$	Vertical positon (height)
K	α	Horizontal wavenumber
k	α_1	Zonal component of wavenumber
l	α_2	Meridional component of wavenumber
ω	ω	Frequency

reproduced by a purely modal model. At the same time, the velocity and temperature coherences are not identical; such coherences cannot be reproduced by a purely WKBJ propagating model. We conclude both standing modes and propagating waves are required. Even though both the standing modes and the propagating waves form complete sets, in forming the cross spectra it is assumed that different waves are statistically independent. In other words, while the set of all propagating waves are complete in the original amplitude space, as a vector decomposition of the spectral space they are certain to be complete only if all waves are allowed to be correlated as well. On the other hand, spatial stationarity implies different wavenumbers are uncorrelated, so perhaps it is sufficient to allow correlations only between the upward and downward propagating waves at a particular wavenumber. What follows here shows the equivalence of 1) correlated upward and downward waves and 2) a mixture of uncorrelated upward propagating waves, downward propagating waves, and standing modes.

Consider the wave field to be a random superposition of four statistically independent components:

$$a\alpha(z) \quad \text{upward propagating wave}$$

$$b\alpha^*(z) \quad \text{downward propagating wave}$$

$$c(i\alpha(z) - i\alpha^*(z)) \quad \text{mode}$$

$$d(\alpha(z) + \alpha^*(z)) \quad \text{antimode},$$

where the antimode (an antinode, i.e., an extreme at z_D) is included for completeness. By assumption these three (or four) internal waves are statistically independent, so the current meter cross spectra can be written

$$\begin{aligned}\langle u_i^* u_j \rangle &= p_i^* p_j[\alpha_i^* \alpha_j \langle a^*a + c^*c + d^*d \rangle \\ &\quad + \alpha_i \alpha_j^* \langle b^*b + c^*c + d^*d \rangle \\ &\quad + \alpha_i^* \alpha_j^* (\langle d^*d \rangle - \langle c^*c \rangle) \\ &\quad + \alpha_i \alpha_j (\langle d^*d \rangle + \langle c^*c \rangle)] \qquad (12a) \\ &= p_i^* p_j[\alpha_i^* \alpha_j \langle A^*A \rangle + \alpha_i \alpha_j^* \langle B^*B \rangle \\ &\quad + \alpha_i^* \alpha_j^* \langle A^*B \rangle + \alpha_i \alpha_j \langle B^*A \rangle]; \qquad (12b)\end{aligned}$$

angle brackets denote an ensemble (statistical) average.

Equation (12b) shows the expansion in terms of the correlated up and down waves. We now define spectral parameters E, Δ, P, Q, where $E = \langle A^*A \rangle + \langle B^*B \rangle$ is the symmetric part of the spectrum, $\Delta = \langle A^*A \rangle - \langle B^*B \rangle$ is the difference between upward and downward propagating waves, $P = \langle A^*B \rangle + \langle B^*A \rangle$ is the modal component of the spectrum, and $Q = i(\langle A^*B \rangle - \langle B^*A \rangle)$ is the antimodal component of the spectrum. We then find

$$\begin{bmatrix} E \\ \Delta \\ P \\ Q \end{bmatrix} = \begin{bmatrix} \langle a^*a \rangle + \langle b^*b \rangle + 2\langle c^*c \rangle + 2\langle d^*d \rangle \\ \langle a^*a \rangle - \langle b^*b \rangle \\ -2\langle c^*c \rangle \\ -2\langle d^*d \rangle \end{bmatrix}. \qquad (13)$$

Equation (13) shows that E is the only parameter that receives contributions from all modes and waves. Consequently, if energy at any given wavenumber can be measured at all, the E component will be measurable. The ability to measure Δ, P, Q then determines whether we can distinguish between upward propagating, downward propagating, and modal solutions. The fact that the GM79 model spectrum is vertically symmetric and effectively propagating ($\Delta = P = Q = 0$) can thus be considered as more of a statement that Δ, P, Q are difficult to measure rather than a statement that the internal wave field is actually vertically symmetric and propagating. In the PEQUOD and LOTUS experiments in particular, and in modern experiments in general, however, the data are sufficient to actually tell us something about the structure of the Δ, P, Q parts of the internal wave field. And it is only with such a generalized view that these modern datasets can be considered consistent with an internal wave spectrum.

Thus, we have changed our theoretical problem (how can a spectrum show both propagating wave and standing mode characteristics) to an estimation problem: how well resolved are E, Δ, P, Q by a given array of sensors? First, consider the cross-spectra for a purely vertical separation. At a particular frequency and horizontal wavenumber, the velocity cross-spectrum Φ_{12}^u and the displacement cross-spectrum Φ_{12}^η for the two depths z_1 and z_2 are given in terms of the spectral parameters by

$$\begin{aligned}&\Phi_{12}^u(\omega, K) \\ &\quad = \langle \tilde{u}_1^* \tilde{u}_2 + \tilde{v}_1^* \tilde{v}_2 \rangle(\omega, K) \qquad (14a) \\ &\quad = \left(1 + \frac{f^2}{\omega^2}\right) \frac{1}{K^2} [\Re(\partial_z \alpha_1^* \partial_z \alpha_2) E + i\Im(\partial_z \alpha_1^* \partial_z \alpha_2) \Delta \\ &\qquad + \Re(\partial_z \alpha_1 \partial_z \alpha_2) P - \Im(\partial_z \alpha_1 \partial_z \alpha_2) Q] \qquad (14b)\end{aligned}$$

and

$$\Phi^{\eta}_{12}(\omega, K) = \langle \tilde{\eta}_1^* \tilde{\eta}_2 \rangle(\omega, K) \quad (14c)$$

$$= \frac{1}{\omega^2}[\Re(\alpha_1^* \alpha_2)E + i\Im(\alpha_1^* \alpha_2)\Delta + \Re(\alpha_1 \alpha_2)P - \Im(\alpha_1 \alpha_2)Q], \quad (14d)$$

where $\Re$, $\Im$ denote real and imaginary parts, respectively. The integral of these expressions over all wavenumber K gives the cross-spectra $\Phi^{u}_{12}(\omega)$ and $\Phi^{\eta}_{12}(\omega)$ between two depths as measured at fixed points (e.g., moored current meters). The problem of calculating cross-spectra is thus reduced to finding an appropriate set of solutions $\alpha(z; \omega, K)$ and performing the integral over wavenumber.

c. Coherence

GM72 argue that most of the results depend only on the local buoyancy frequency $N(z)$ and therefore it does not matter which model $N(z)$ profile is chosen. This effectively chooses a WKBJ approximate solution for α [we take the hydrostatic limit $\omega \ll N(z)$ as well]:

$$\alpha(z) = \left(\frac{\omega^2 - f^2}{N(z)}\right)^{1/2} e^{i\int^z m(z')dz'}, \quad (15)$$

where

$$m(z) = \frac{N(z)}{\sqrt{\omega^2 - f^2}} K, \quad (16)$$

and

$$\alpha_z(z) = im(z)\alpha(z). \quad (17)$$

GM72 also assume $\Delta = P = Q = 0$; that is, the spectrum is vertically symmetric and the top and bottom boundary conditions are unimportant. By defining a coordinate ψ, we can get quite simple expressions for the moored sensor cross-spectra: ψ is given by

$$\psi_{12} = \int_{z_1}^{z_2} \frac{N(z')}{\sqrt{\omega^2 - f^2}} dz' \quad (18)$$

and the cross-spectra for velocity and displacement are

$$\Phi^{u}_{12}(\omega) = \left(1 + \frac{f^2}{\omega^2}\right)(N(z_1)N(z_2))^{1/2} \times \int_0^{\infty} \cos K\psi_{12} E(\omega, K) dK \quad (19a)$$

and

$$\Phi^{\eta}_{12}(\omega) = \left(1 - \frac{f^2}{\omega^2}\right)(N(z_1)N(z_2))^{-1/2} \times \int_0^{\infty} \cos K\psi_{12} E(\omega, K) dK. \quad (19b)$$

These expressions for cross-spectra have identical dependence on the equivalent vertical coordinate ψ; thus the velocity and displacement coherences are identical:

$$\gamma(z_1, z_2, \omega) e^{i\phi(z_1, z_2, \omega)} = E^{-1}(\omega) \int_0^{\infty} dK E(\omega, K) \cos K\psi_{12}. \quad (20)$$

These expressions can be analytically evaluated for the continuous spectral form (2) used in GM79: there the coherence $\gamma(z_1, z_2, \omega) = C_{\text{cont}}(K_* \psi_{12})$ is the cosine transform of (3), namely, a purely real exponential function of scaled separation, $C_{\text{cont}}(X) = e^{-|X|}$.

By comparing Eqs. (14b) and (14d), one can see that the MVC calculated from velocities and the MVC calculated from displacement are the same only because $P = Q = \Delta = 0$ and the WKBJ vertically propagating solutions have the property that the ratio

$$\frac{\alpha_z^*(z_1)\alpha_z(z_2)}{K^2 \alpha^*(z_1)\alpha(z_2)} \quad (21)$$

is independent of K.

The top and bottom boundary conditions are no normal flow at a rigid top ($z = 0$) and rigid (and flat) bottom ($z = z_D$). This implies that our particular solution (11) satisfies

$$G(0) = G(z_D) = 0. \quad (22)$$

Imposing the bottom boundary condition means that $P = -E$; that is, the upward and downward propagating waves become phase locked. Imposing an upper boundary condition as well restricts $K\psi_D(0)$ to be an integral multiple of π,

$$K\psi_D(0) = K \frac{D\bar{N}}{\sqrt{\omega^2 - f^2}} = \pi j, \quad (23)$$

$\bar{N}$ being the depth-averaged buoyancy frequency. The equivalent exponential profile has $bN_0 = D\bar{N}$ (Blumenthal 1987).

Consider a discrete version of the function $C(X)$ defined to be

$$C_{\text{sum}}(X) = \sum_{j=1}^{\infty} H(K_j) \cos\left(\frac{K_j}{K_*} X\right), \quad (24)$$

where

$$H(K_j) = \frac{E(\omega, K_j)dK_j}{E(\omega)}. \quad (25)$$

This discrete version corresponds to GM79; the continuous version to Desaubies (1976). Comparing Eqs. (24) and (20) reveals that $C_{\text{sum}}(K_* \psi)$ and $C_{\text{cont}}(K_* \psi)$ differ in two ways: it is a sum rather than an integral, and the sum starts from mode 1 rather than wavenumber zero. Using the expression for $C(X)$ in place of the expression in Eq. (20) modifies the MVC such that it includes the discretization of wavenumber effect of

imposing boundary conditions. (The effects of phase locking are considered in the next section.)

Figure 7 compares three versions of $C(X)$ that use the wavenumber form chosen in GM79: a direct evaluation of Eq. (24) using Eq. (2) (C_{sum}), and two continuous integral approximations for $C(X)$, C_{cont} and

$$C_{\text{cut}}(X) = \frac{e^{-|X|} - \epsilon}{1 - \epsilon}, \tag{26}$$

where $\epsilon = 0.106$ is the contribution that the zero wavenumber mode makes to the integral. The plot shows that the sum and the cutoff integral give identical results. Consequently, as far as the discretization effect of boundary conditions is concerned, the imposition of boundary conditions could be modeled as a low wavenumber cutoff of a continuous spectrum. The important distinction between the continuous and discrete cases is that while the first expression approaches 0 for large X, the second expression approaches -0.1. This limiting value of -0.1 can be conceptualized as the signature of the missing zeroth mode. Were the zeroth mode present in the sum, this limiting value would be zero, due to the presence of many modes. On the other hand, were the zeroth mode present by itself, motions would be perfectly coherent for all depth pairs with no phase difference. Thus, in the actual case, when the zeroth mode is absent, but all the other modes are present, what is seen is the coherence structure that when added to the zeroth mode gives zero, that is, a small amount of energy with 180° phase differences at long separations.

A modified $C(X)$ function alone, does not lead to different coherence structures for velocity and displacement. To model that difference, the effects of phase locking must be included. Using $P = -E$ in (14b) and (14d) gives

$$\Phi^{u}_{12}(\omega) = \left(1 + \frac{f^2}{\omega^2}\right)[N(z_1)N(z_2)]^{1/2}(C[K_*\psi_{12}] + C[K_*(\psi_{D1} + \psi_{D2})])E(\omega) \tag{27a}$$

and

$$\Phi^{\eta}_{12}(\omega) = \left(1 - \frac{f^2}{\omega^2}\right)[N(z_1)N(z_2)]^{-1/2}(C[K_*\psi_{12}] - C[K_*(\psi_{D1} + \psi_{D2})])E(\omega). \tag{27b}$$

The effect of the phase locking is to add an extra term to the purely propagating solution. The term is a function of the average scaled depth $\psi_{av} = \frac{1}{2}(\psi_{D1} + \psi_{D2})$ of the two points being considered, which means that the wave field is no longer vertically homogeneous. As long as the two depths z_1 and z_2 being considered are sufficiently far from the boundaries (according to Fig. 8, sufficiently far means that the sum of their WKBJ stretched separations from a boundary is greater than 1500 m and less than 6500 m), the added term will be

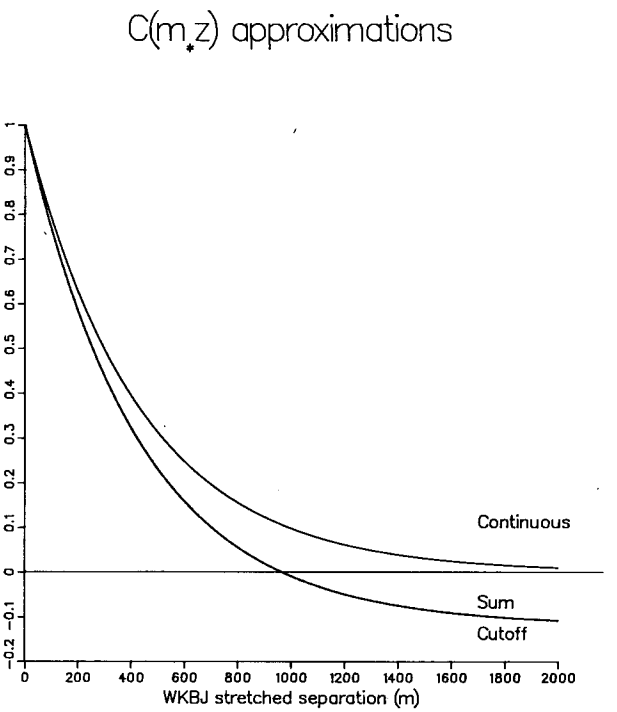

FIG. 7. The three lines give three approximations to the function $C(X)$, a function which gives the vertical coherence for an internal wave field that is purely vertically propagating. The functions are plotted against WKBJ stretched separation ζ, which is proportional to the equivalent vertical coordinate ψ, where $m_*\zeta = K_*\psi$ and m_* is 2.33×10^{-3} m^{-1}. The plot shows that the continuous spectrum with a low-wavenumber cutoff is indistinguishable from the discrete sum of modes where mode 0 is absent.

the limiting value of $C(X)$ for large argument. That limiting value depends on the choice of function $C(X)$. Choosing C_{sum} (which excludes the zeroth mode) means that the limiting value is -0.1 and there is a difference between velocity and displacement cross-spectra. Thus, both the effects of phase locking and of the missing zeroth mode are required before there will be differences between the velocity coherence and the temperature coherence of the character seen in PEQUOD's long-separation coherences.

Along with the above two modifications, GM predicts that for very long separations the velocity coherence is 0.2 with a phase difference of 180°, while the displacement cross-spectra goes to zero. In terms of WKBJ stretched depth, the crossover point where the velocity phase difference goes from zero (for short separations) to 180° (for long separations) occurs at 800 m, while the temperature phase difference is always zero. This phase information matches the simple characterizations of the phase differences from temperature and velocity observed in PEQUOD. The model also predicts that the displacement cross-spectra at 800-m WKBJ stretched depth should be twice what the vertically propagating model predicts, which also is consistent with observations at 1000-m WKBJ stretched

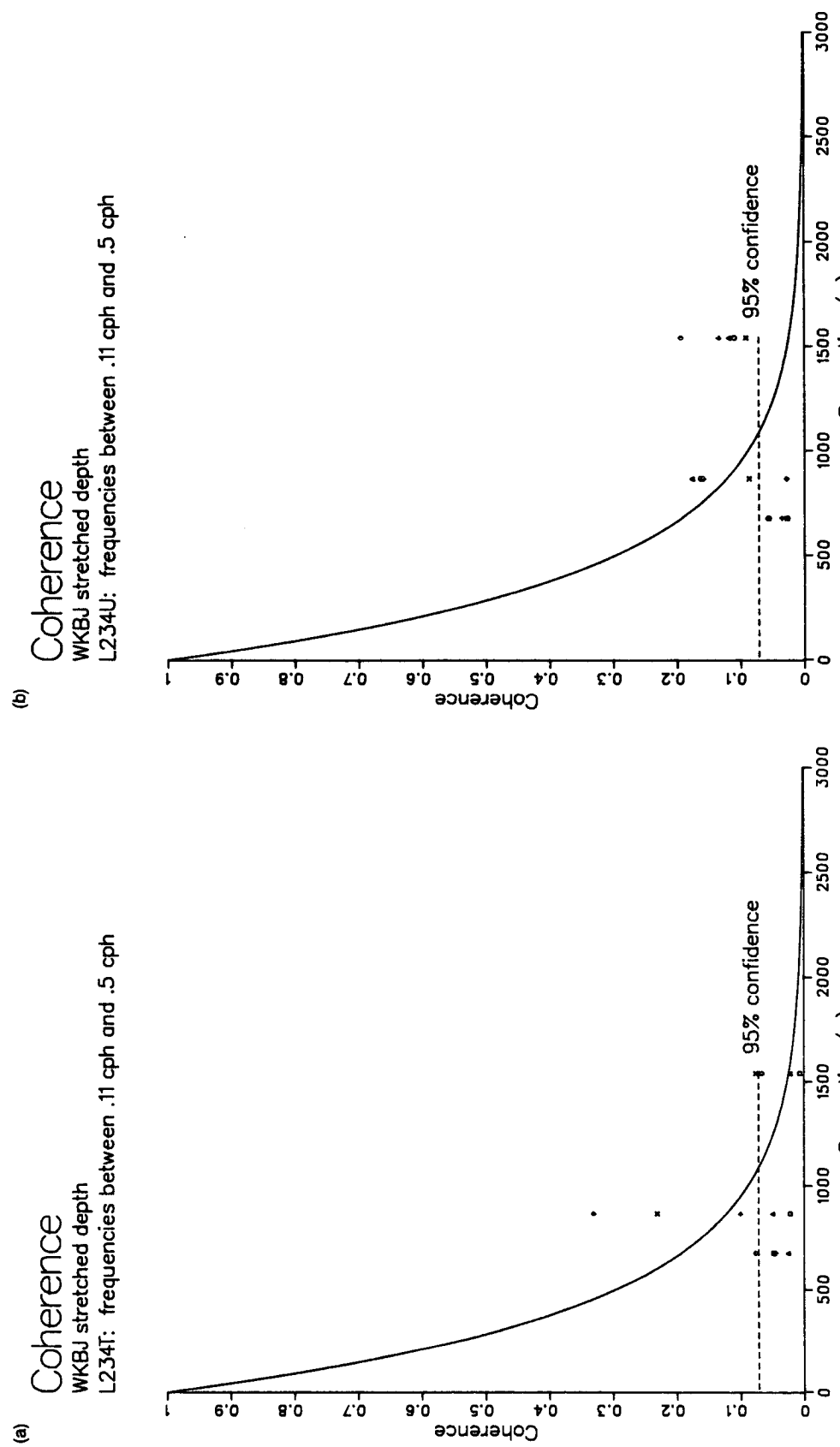

FIG. 8. Vertical coherence and phase calculated from LOTUS as a function of WKBJ-stretched separation for frequencies between 0.1 cph and 0.5 cph. Each symbol corresponds to a different frequency bin. The lowest frequency bin centered at 0.170 cph. The frequency bin width is $2/15$ cph. The plots are: (a) temperature coherence, (b) zonal-velocity coherence, (c) temperature phase, and (d) zonal-velocity phase.

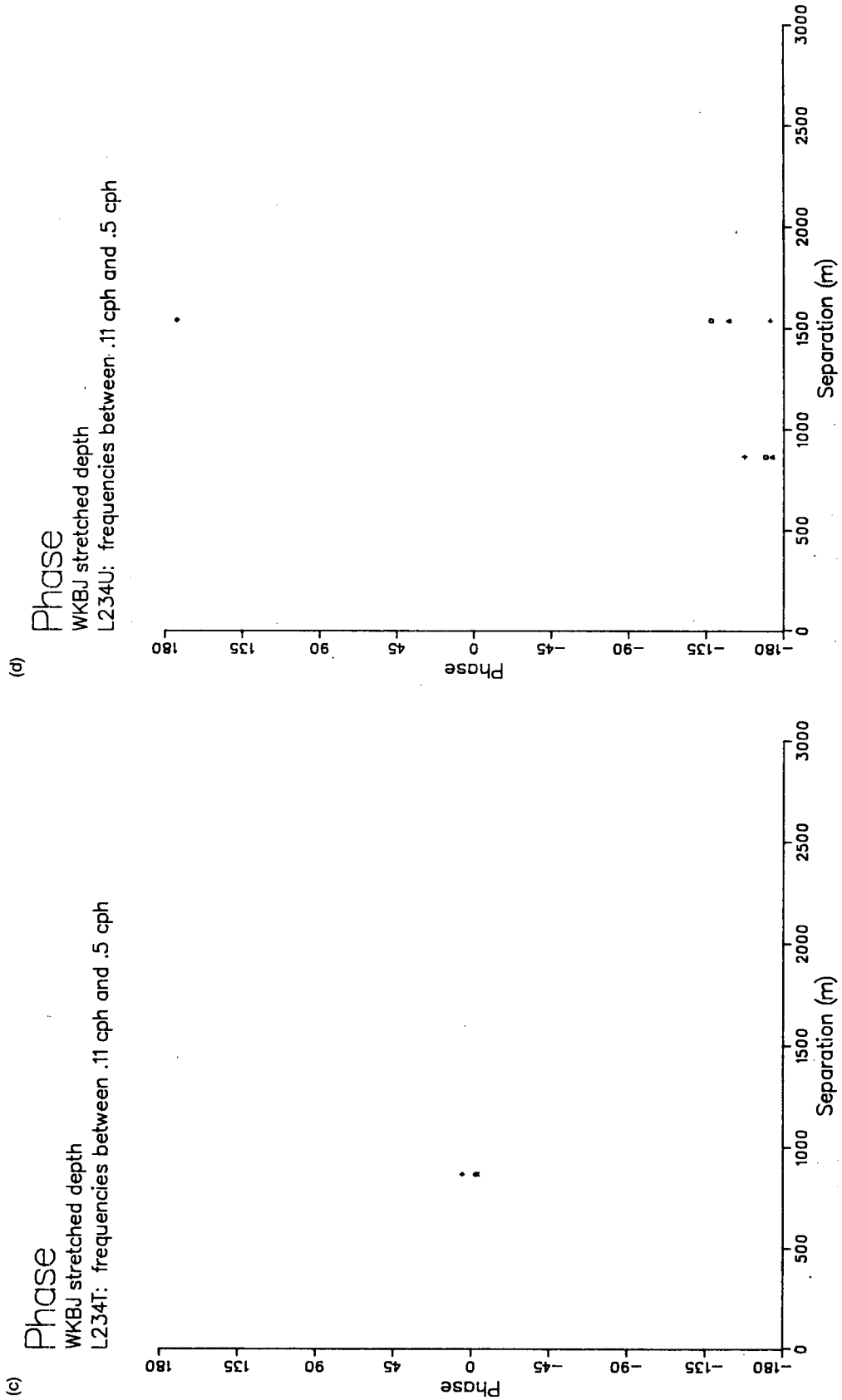

FIG. 8. (*Continued*)

depth. Furthermore, the prediction says that the coherences at a WKBJ stretched separation of 1500 m are closer to the coherences at a WKBJ stretched separation of 2500 m than to the coherences at a WKBJ stretched separation of 1000 m, something also seen in the observations. Finally, these model predictions are such that the predicted coherences at short separations are roughly the same as the GM79 predictions modified by finestructure, so that all the data used in designing GM79 are also consistent with the modified model.

6. Coherence and phase from LOTUS

To see whether these modal effects can be seen in midlatitude data, we consider coherences calculated from four of the second-year Long Term Upper Ocean Study (LOTUS) current meter records. These records also have the advantage that they are not subject to the direction aliasing that affects the PEQUOD measurements, and the records have better high-frequency resolution. Details of the mooring structure are given in a LOTUS technical report (Tarbell et al. 1985). The instruments used are located at depths 1000 m, 1500 m, 2500 m and 4000 m. The mooring is in 5200 m of water, thus all the instruments are well away from the boundaries. The bottom is flat, in the Hatteras Abyssal Plain. The upper (1000 m) instrument is in the bottom part of the thermocline, while the other instruments are well away from any rapid changes in the buoyancy frequency. It turns out that all the coherences between the 1000-m instrument and the other instruments are very low, not at all consistent with the PEQUOD observations. This lack of coherence is probably due to the rapidly changing buoyancy frequency at 1000 m, a situation which is not included in the model of modal effects. The 1000-m record is therefore omitted from the remaining comparisons.

Table 4 gives the local buoyancy frequency and the WKBJ stretched separations for the LOTUS instruments used. Omitting the 1000-m instrument leaves estimates at 674-m, 864-m, and 1538-m WKBJ stretched separations; these are smaller separations than are available from the PEQUOD mooring.

Figure 8 shows the temperature coherences for the three deep instruments. The temperature records are for the most part incoherent. The significant coherences that do exist are close to the local buoyancy frequency. For example, the 2500- and 4000-m records are coherent for most of the frequencies between 0.1 and 1 cph. This fairly broad peak is probably associated with frequencies approaching the local buoyancy frequency. All the nearest neighbor pairs show some sort of peak near the local buoyancy frequency, though none of the others are as broad as the peak in the 2500 m–4000 m case. Essentially the temperature coherences are not conclusive: they are consistent with either a modal or propagating internal wave model.

The velocity coherences, on the other hand, do show features similar to what was found in the PEQUOD data. Both zonal and meridional velocities (zonal velocity is shown) have a statistically significant coherence with a 180° phase difference for long separations in the 0.1 to 0.5 cph frequency band. There are no energy peaks at local buoyancy frequencies, though there are significant coherence peaks at frequencies above the buoyancy frequency. The 4000-m records are significantly coherent with both 1500- and 2500-m records starting at frequencies below 0.1 cph and continuing throughout the internal wave band. These coherences correspond to phase differences of 180°. The 1500-m velocity records, on the other hand, are not coherent with the 2500-m records except at frequencies near the local buoyancy frequency. This is similar to the features in the PEQUOD data, except that it requires a model with a phase crossover closer to 700-m WKBJ stretched separation than the 900 m found with the PEQUOD data.

Thus the LOTUS velocity data are roughly consistent with low wavenumber energy being modal in character. The temperature data are not so clear, mainly because the deep water buoyancy frequency is so low (0.6 cph) that it is hard to separate the effects seen in the PEQUOD data from near-buoyancy frequency effects (Desaubies 1975).

7. Summary of coherence results

The coherence and phase as a function of vertical separation computed from both PEQUOD and LOTUS data show distinct differences from the GM predictions at separations of 1000 m and longer. Tem-

TABLE 4. Frequency grid and WKBJ stretched separations for LOTUS instruments.

Depth (m)	$\bar{N}$ (cph)	WKBJ depth (m)	WKBJ separations				Symbol	Frequency (cph)
			1000 m	1500 m	2500 m	4000 m		
							□	.1700
1000	1.384	1000					△	.2367
1500	0.674	1692	692				+	.3033
2500	0.576	2366	1366	674			×	.3700
4000		3230	2230	1538	864		◇	.4367

perature coherence is 0.2 ± 0.08 at 1000-m separation, significantly higher than the GM prediction, but it drops off quickly so that by 1500-m separations the coherence is indistinguishable from zero. In contrast, velocity coherence is indistinguishable from zero at 1000-m separation, but increases for longer separations so that it is roughly 0.2 at 2500-m separations. Temperature phase can be characterized roughly as zero for all separations by ignoring some of the phases that correspond to low coherences, while velocity phase is characterized roughly as 180° for all separations greater than 1000 m. These characterizations can be understood in terms of a modified GM model that includes two effects that are a result of imposing top and bottom boundaries: 1) phase locking between upward and downward propagating waves to form modes and 2) a low wavenumber cutoff such that there is little energy below the first baroclinic mode.

This phase-locked behavior throughout the frequency range is in contrast to earlier experimental evidence for modal character in the internal wave field (Desaubies 1975; Pinkel 1975) that finds phase locking only near the local buoyancy frequency. These earlier studies did not examine closely the lower frequencies or larger scales.

Determining the low-wavenumber cutoff and, more generally, determining the low-wavenumber distribution of energy are important because the low modes contain most of the internal wave energy. Such an effect is even more pronounced when considering energy fluxes, because not only are the low modes more energetic, they are also faster, thus making proportionally an even stronger contribution to the energy flux. The GM modifications discussed so far have only been selectively compared to the data: we have not partitioned the energy between a model spectrum and noise to get a full accounting of all the energy measured. In particular, the model is still vertically symmetric and horizontally isotropic: such a model has net energy fluxes that are identically zero and is inconsistent with the nearly 90° phases that were seen at some frequencies. A spectral inversion that directly estimates E, Δ, P, Q for PEQUOD (Blumenthal 1987) makes such a quantitative allocation and does, in fact, find significant vertical fluxes Δ.

In hindsight, the message of the PEQUOD and LOTUS datasets is not particularly surprising: high wavenumbers do behave much as GM79 predicts but low modes do not, and low modes contain most of the energy. The experiments show that the energy at long vertical scales shows some modal characteristics, exactly as linear theory predicts. For low modes this is not surprising since they have fast phase speeds c (thus they are more linear in a u/c sense), and nonlinearities (scattering) would have to be extremely strong in order to completely scatter a wave in one wavelength (half a wavelength for the first mode). On the other hand, dissipation does act on these waves, and to the extent that they transport energy, there is a phase difference between top and bottom. The mixture of standing modes and propagating waves is thus the spectral representation of the balance between the phase locking that the boundary causes and the scattering/friction/forcing that destroys that phase information.

Comparison of estimates of the energy contained in the internal wave field (Olbers 1983; Briscoe 1983) with the size of potential sources of energy in the internal wave field $O(10^{-3}\ \mathrm{W\ m^{-2}})$ shows that the net fluxes carried by the internal wave field are much smaller than the uniformly distributed (standing) energy. Thus Δ, which is proportional to the net vertical energy flux, is much smaller than E, and consequently the imaginary part of cross-spectra will be quite small in comparison to the real part. A year-long time series has an error level in suitably averaged spectral estimates of $0.5 \times 10^{-3}\ \mathrm{W\ m^{-2}}$ (Blumenthal 1987), so a persistent flux could barely be detected. A more short-lived vertical flux, however, such as that from a storm, cannot be detected (Briscoe 1983). It is only by measuring these small components of the spectrum, however, that we can measure how energy is transported by the internal wave field.

Acknowledgments. This work was supported under grants from the National Science Foundation and the Office of Naval Research administered through the Massachusetts Institute of Technology, Grants numbered NSF-89076, ONR-88914, NSF-91002, NSF-94971, and NSF-93661.

REFERENCES

Blumenthal, M. B., 1987: Interpretation of equatorial current meter data as internal waves. Ph.D. thesis, Massachusetts Institute of Technology/Woods Hole Oceanographic Institution, WHOI-87-7, 381 pp.

Briscoe, M. G., 1975: Preliminary results from the trimoored internal wave experiment (IWEX). *J. Geophys. Res.*, **80,** 3872–3884.

——, 1977: On current finestructure and moored current meter measurements of internal waves. *Deep-Sea Res.*, **24,** 1121–1131.

——, 1983: Observations on the energy balance of internal waves during JASIN. *Phil. Trans. Roy. Soc. London, A,* **308,** 427–444.

——, 1984: The monthly variability of upper-ocean internal wave energy: A progress report on the correspondence with wind stress. *Internal Gravity Waves and Small-Scale Turbulence. Proc. of the 'Aha Huliko'a Hawaiian Winter Workshop University of Hawaii at Manoa, January 17–20 1984* P. Müller and R. Pujalet, Eds., University of Hawaii, 129–150.

——, and R. Weller, 1984: Preliminary results from the long-term upper-ocean study (LOTUS). *Dyn. Atmos. Oceans,* **8,** 243–265.

Cairns, J., and G. Williams, 1976: Internal wave observations from a midwater float, 2. *J. Geophys. Res.*, **81,** 1943–1950.

Desaubies, Y., 1975: A linear theory of internal wave spectra and coherences near the Väisälä frequency. *J. Geophys. Res.*, **80,** 895–899.

——, 1976: Analytical representation of internal wave spectra. *J. Phys. Oceanogr.*, **6,** 976–981.

Eriksen, C. C., 1985: Some characteristics of internal gravity waves in the equatorial pacific. *J. Geophys. Res.*, **90,** 7243–7255.

——, 1988: Variability in the upper-ocean internal wave field at a Sargasso Sea site. *J. Phys. Oceanogr.*, **18,** 1495–1513.

Garrett, C., 1991: Paradigm lost? *Dynamics of Oceanic Internal Gravity Waves. Proc. of the 'Aha Huliko 'a Hawaiian Winter*

Workshop University of Hawaii at Manoa, January 15–18, 1991, P. Müller and D. Henderson, Eds., University of Hawaii, School of Ocean and Earth Science and Technology Special Publication, 433–449.

——, and W. Munk, 1972: Space–time scales of internal waves. *Geophys. Fluid Dyn.*, **2**, 225–264.

——, and ——, 1975: Space–time scales of internal waves: A progress report. *J. Geophys. Res.*, **80**, 291–297.

Gent, P., and J. Luyten, 1985: How much energy propagates vertically in the equatorial oceans? *J. Phys. Oceanogr.*, **15**, 997–1007.

Levine, M., 1984: Internal wave climatology: An update. *Internal Gravity Waves and Small-Scale Turbulence. Proc. of the 'Aha Huliko 'a Hawaiian Winter Workshop University of Hawaii at Manoa, January 17–20 1984*, P. Müller and R. Pujalet, Eds., University of Hawaii, Hawaii Institute of Geophysics Special Publication, 151–162.

Luyten, J., and J. Swallow, 1976: Equatorial undercurrents. *Deep Sea Res.*, **23**, 999–1001.

McComas, C., and F. Bretheron, 1977: Resonant interaction of oceanic internal waves. *J. Geophys. Res.*, **82**, 1397–1412.

Munk, W., 1981: Internal waves and small scale processes. *Evolution of Physical Oceanography*, B. Warren and C. Wunsch, Eds., The MIT Press, 264–291.

Olbers, D., 1983: Models of the oceanic internal wave field. *Rev. Geophys. Space Phys.*, **21**(7), 1567–1606.

Philander, G., 1978: Forced oceanic motions. *Rev. Geophys. Space Phys.*, **16**, 15–46.

Pinkel, R., 1975: Upper ocean internal wave observations from flip. *J. Geophys. Res.*, **80**, 3892–3910.

——, 1984: Doppler sonar observations of internal waves: The wavenumber–frequency spectrum. *J. Phys. Oceanogr.*, **14**, 1249–1270.

Roth, M., M. Briscoe, and C. McComas, 1981: Internal waves in the upper ocean. *J. Phys. Oceanogr.*, **11**, 1234–1247.

Tarbell, S., E. Montgomery, and M. Briscoe, 1985: A compilation of moored current meter and wind recorder data volume XXXVIII Long-Term Upper Ocean Study (LOTUS) (moorings 787 788 789 790 792) April 1983–May 1984. WHOI Tech. Rep. WHOI-85-39, Woods Hole Oceanographic Institution, Woods Hole, MA.

Voorhis, A., J. R. Luyten, G. Needell, and J. Thomson, 1984: Wind-forced variability of upper ocean dynamics in the central equatorial Pacific during PEQUOD. *J. Phys. Oceanogr.*, **14**, 615–622.

Wijesekera, H. W., and T. M. Dillon, 1991: Internal waves and mixing in the upper equatorial Pacific Ocean. *J. Geophys. Res.*, **96**(C4), 7155–7125.

Wunsch, C., 1976: Geographic variability of the internal wave field: A search for sources and sinks. *J. Phys. Oceanogr.*, **6**, 471–485.

——, and J. Dahlen, 1974: A moored temperature and pressure recorder. *Deep-Sea Res.*, **21**, 145–154.

——, and S. Webb, 1979: The climatology of deep ocean internal waves. *J. Phys. Oceanogr.*, **9**, 235–243.